Mon. Not. R. Astron. Soc. **421,** 3316–3324 (2012) doi:10.1111/j.1365-2966.2012.20555.x

Observations and modelling of pulsed radio emission from CU Virginis

K. K. Lo,[1,2,3★] J. D. Bray,[2,4] G. Hobbs,[2] T. Murphy,[1,3,5] B. M. Gaensler,[1,3] D. Melrose,[1] V. Ravi,[2,6] R. N. Manchester[2] and M. J. Keith[2]

[1]*Sydney Institute for Astronomy, School of Physics, The University of Sydney, NSW 2006, Australia*
[2]*Australia Telescope National Facility, CSIRO Astronomy and Space Science, PO Box 76, Epping, NSW 1710, Australia*
[3]*ARC Centre of Excellence for All-sky Astrophysics (CAASTRO), The University of Sydney, NSW 2006, Australia*
[4]*School of Chemistry & Physics, The University of Adelaide, SA 5005, Australia*
[5]*School of Information Technologies, The University of Sydney, NSW 2006, Australia*
[6]*School of Physics, University of Melbourne, Parkville, VIC 3010, Australia*

Accepted 2012 January 13. Received 2012 January 12; in original form 2011 June 23

ABSTRACT

We present 13 and 20 cm radio observations of the magnetic chemically peculiar star CU Virginis taken with the Australia Telescope Compact Array. We detect two circularly polarized radio pulses every rotation period which confirm previous detections. In the first pulse, the lower frequency emission arrives before the higher frequency emission and the ordering reverses in the second pulse. In order to explain the frequency dependence of the time between the two pulses, we construct a geometric model of the magnetosphere of CU Virginis, and consider various emission angles relative to the magnetic field lines. A simple electron cyclotron maser emission model, in which the emission is perpendicular to the magnetic field lines, is not consistent with our data. A model in which the emission is refracted through cold plasma in the magnetosphere is shown to have the correct pulse arrival time frequency dependence.

Key words: magnetic fields – radiation mechanisms: non-thermal – stars: individual: CU Virginis – stars: rotation – radio continuum: stars.

1 INTRODUCTION

CU Virginis (HD 124224, hereafter CU Vir) is one of the best studied Ap stars. It is very nearby (distance of only 80 pc) and is a fast rotator (period of around 0.52 d; Deutsch 1952). Its strong magnetic field (polar magnetic field of ∼3 kG) places it in the category of magnetic chemically peculiar (MCP) stars. Like other MCP stars, its effective magnetic field has been observed to vary with rotational phase (Borra & Landstreet 1980). In addition, MCP stars are known radio emitters (Drake et al. 1987; Linsky, Drake & Bastian 1992; Leone, Trigilio & Umana 1994) and their radio emission has been observed to modulate with rotational phase (Leone 1991; Leone & Umana 1993). This quiescent radio emission is believed to be gyrosynchrotron radiation emitted by mildly relativistic (Lorentz factor of $\gamma \leq 2$) electrons trapped in the magnetosphere (Drake et al. 1987). Trigilio et al. (2004) constructed a three-dimensional model to explain the rotational modulation of the quiescent radio emission from an MCP star and Leto et al. (2006) successfully applied it to CU Vir.

Circular polarization in the radio emission was detected at the 10 per cent level by Leone, Umana & Trigilio (1996), which is expected for the gyrosynchrotron emission. Subsequently, Trigilio et al. (2000) discovered that CU Vir produces two 100 per cent circularly polarized radio pulses every rotation period which cannot arise from the gyrosynchrotron emission mechanism.

The observed radio flux for CU Vir across one rotation period is hereafter described as the 'pulse profile'. The two components in the pulse profile are referred to as the 'leading' and 'trailing' pulses. Similar pulse profiles have been observed from CU Vir in the 13 and 20 cm observing bands (Trigilio et al. 2000, 2008, 2011; Ravi et al. 2010) where observations were separated by almost a decade. CU Vir is the only MCP star that has been observed to emit radio pulses.

Trigilio et al. (2000) proposed electron cyclotron maser (ECM) as the emission mechanism for the pulsed radio emission. Plasma radiation due to Langmuir waves was ruled out (Trigilio et al. 2008) because of the low electron density in the emission region as modelled by Leto et al. (2006) and the observation that requires the radiation to be tightly beamed. ECM can produce radiation with high directivity and 100 per cent circular polarization. In the 'loss cone' model of ECM (Melrose & Dulk 1982), ECM emission forms a hollow cone at a large angle (70°–85°) to the magnetic field lines, and occupies a narrow frequency band close to a harmonic of the cyclotron frequency. Although ECM is narrow band, the relatively wide band of the observation can be explained if the emission region spans a range of magnetic field strengths.

A simple ECM model does not explain all the features of the pulsed radio emission from CU Vir. For instance, in the 20 cm observing band, the leading and trailing pulses are separated by ∼5 h.

★E-mail: kitty@physics.usyd.edu.au

Table 1. Summary of ATCA observation parameters.

Date	Start time (UT)	Frequency (MHz)	Bandwidth (MHz)	ATCA configuration	Integration time (h)	Phase calibrator	Reference
1999 May 29	06:57	1384, 2496	128, 128	6A	9.3	B1406−076	Trigilio et al. (2008)
1999 August 29	01:12	1384, 2496	128, 128	6D	9.0	B1406−076	Trigilio et al. (2008)
2008 October 30	21:06	1384, 2368	128, 128	6A	9.0	B1416+067	Ravi et al. (2010)
2009 December 23	18:13	1503	742	6A	1.2	B1406−076	This work
2009 December 24	18:11	2335	678	6A	1.6	B1406−076	This work
2009 December 25	20:01	1503, 2335	742, 678	6A	1.9	B1406−076	This work
2009 December 26	20:13	1503, 2335	742, 678	6A	2.4	B1406−076	This work
2010 May 19	08:02	1503, 2335	742, 678	6C	8.2	B1416+067	This work
2010 Jun 15	06:41	1503	742	6C	9.2	B1402−012	This work

In the 13 cm observing band, the leading pulse was not seen in observations by Trigilio et al. (2008), but was seen a decade later by Ravi et al. (2010). In contrast to the variability of the leading pulse, the trailing pulse shows remarkable stability over more than a decade in both observing bands. The trailing pulse at 13 cm is always observed to arrive earlier than the corresponding 20 cm pulse. Trigilio et al. (2008) postulated that this has a geometric explanation, which is related to where the pulse originates in the magnetosphere. The discovery from Ravi et al. (2010) that the leading 13 cm pulse arrives later than the corresponding 20 cm pulse agrees with this interpretation and suggests that both pulses come from the same magnetic pole of the star. However, until now, existing data do not provide enough frequency coverage to study the pulse profile in detail as a function of observing frequency. Here we present new data with more complete frequency coverage over the 13 and 20 cm observing bands and demonstrate with our modelling that an ECM emission model, without propagation effects, cannot explain the observations. In a recent paper, Trigilio et al. (2011) suggest that the frequency dependence of the pulse arrival time arises from frequency-dependent refraction of the radiation through the stellar magnetosphere. In this paper, we have analysed the frequency-dependent refraction model in more detail.

The structure of the paper is as follows. In Section 2, we present the observing and analysis techniques used to detect time-varying emission from CU Vir with the Australia Telescope Compact Array (ATCA) and present our observational results. In Section 3, we discuss our modelling and show how it relates to our observations.

2 OBSERVATIONS AND DATA ANALYSIS

We observed CU Vir with the ATCA on six separate occasions (2009 December 23–26, 2010 May 19 and June 15). The observations in 2009 December were only 2 h each in length because they were taken during unallocated telescope time. For these short observations, we predicted the arrival time of the trailing pulse using the ephemeris from Ravi et al. (2010) and timed our observation accordingly. We were allocated time for the 2010 May and June epochs and hence were able to observe for about 9 h continuously. A summary of the observation parameters is given in Table 1.

All our observations were taken with the Compact Array Broadband Backend (CABB; Wilson 2011), which offers a bandwidth of up to 2 GHz per intermediate frequency and polarization. However, the maximum bandwidth in our 20 and 13 cm observing bands was limited to around 700 MHz because our observations were taken before the upgrade was fully completed. Furthermore, it was not possible to observe at 20 and 13 cm simultaneously. To maximize the apparent bandwidth, we switched between the 20 and 13 cm bands every few minutes in the 2009 December 25–26 and 2010 May 19 epochs. Complex visibility data in four polarizations were recorded for 15 baselines with a sampling time of 10 s.

We also made use of archival (pre-CABB) ATCA data to supplement our analysis. Altogether, we analysed eight epochs of data at 20 cm and seven epochs at 13 cm as summarized in Table 1. In column order, we provide the date of observation, the observing frequencies used,[1] the available bandwidth, the configuration of the ATCA,[2] the total integration time, the phase calibrator used and a reference for the data.

We calibrated our data using the standard MIRIAD software package (Sault, Teuben & Wright 1995).[3] The flux amplitude scale and the bandpass response were determined from the backup ATCA primary calibrator 0823−500. Observations of a bright compact radio source (as listed in Table 1) for 1.5 min every 20 min were used to calibrate the complex gains and leakage between the orthogonal linear feeds in each antenna. Radio frequency interference (RFI) was removed from the visibilities using the flagging tool MIRFLAG.

To obtain light curves, we first imaged the field in the standard way. Then, we took the CLEAN components of each source, masking the location of CU Vir, and subtracted them from the visibility data using the MIRIAD task UVMODEL. We then shifted the phase centre of the visibilities to the location of CU Vir and measured the flux density directly from the visibilities by vector averaging their real components in time bins of 3 min.

2.1 Pulse profile

The 20 and 13 cm Stokes V pulse profiles from our observations, along with other archival epochs, are shown in Figs 1 and 2, respectively. The Stokes V flux densities are plotted against rotational phase using the ephemeris from Trigilio et al. (2011) and adjusted for the rotation of the Earth around the Sun. We have used the rotation period $P = 0.520\,716\,01$ d from Trigilio et al. (2011) to align the light curves and set phase zero, in HJD, to be $245\,0966.3601 + EP$, where E is the number of epochs. As can be seen in Figs 1 and 2, the rotation period is a good fit to our data as the pulses are aligned in phase.

[1] We refer to the 1384 MHz pre-CABB and 1503 MHz CABB frequencies as the 20 cm band, and the pre-CABB 2496 MHz and CABB 2335 MHz frequencies as the 13 cm band.

[2] In all cases, a maximum baseline of 6 km was used. The various labels (6A, 6C and 6D) refer to different antenna spacings, which are defined at http://www.narrabri.atnf.csiro.au/operations/array_configurations/configurations.html.

[3] http://www.atnf.csiro.au/computing/software/miriad/

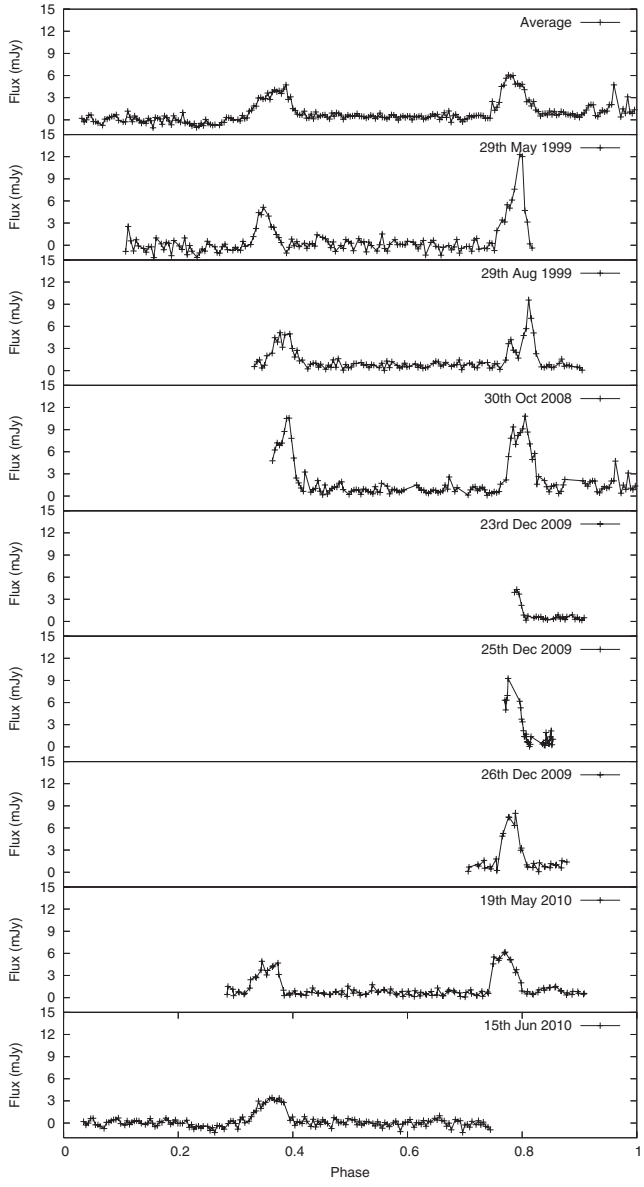

Figure 1. 20 cm Stokes *V* pulse profiles from all epochs listed in Table 1 aligned using the rotation period from Trigilio et al. (2011).

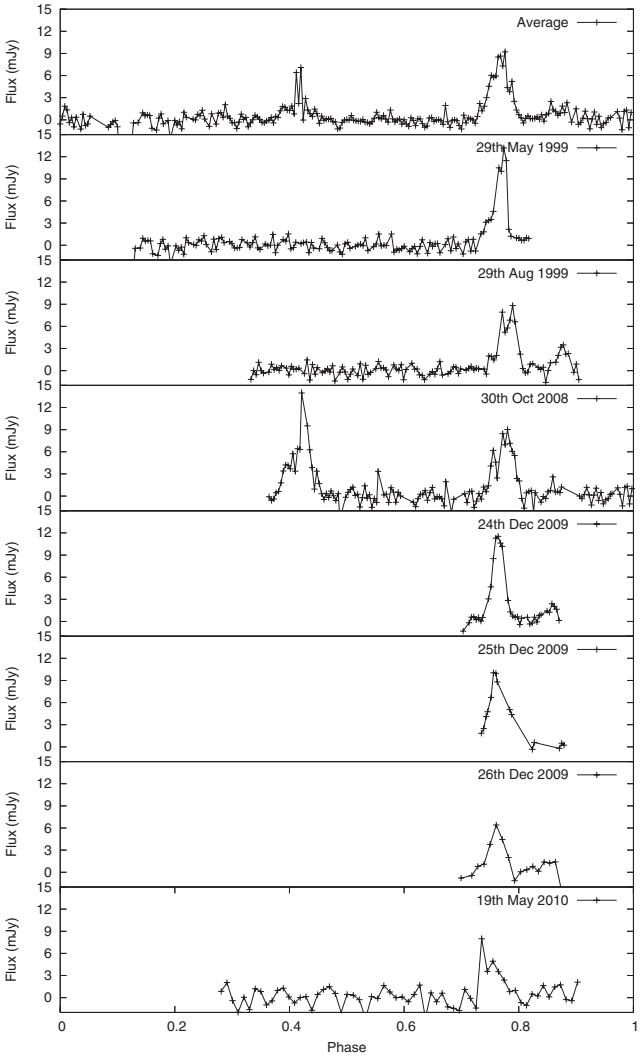

Figure 2. 13 cm Stokes *V* pulse profiles from all epochs listed in Table 1 aligned using the rotation period from Trigilio et al. (2011).

In the 2010 May epoch, we detected both the leading and trailing pulses. The time between them is 5.20 ± 0.05 h in the 20 cm observing band. This is similar to the pulse separation time determined by Trigilio et al. (2000) and Ravi et al. (2010) in earlier epochs. In Fig. 3, we have juxtaposed measurement of the effective magnetic field from Pyper et al. (1998) with the average Stokes *V* pulse profiles. Assuming a dipolar field structure, and taking negative effective magnetic field to mean that the field lines point into the star, the magnetic south pole is closest to our line of sight during the shorter of the two pulse separations.

We did not detect the 13 cm leading pulse, which had been detected in 2008. Although the trailing pulse was detected in all epochs for which we have data at the relevant phase, the peak flux density varied between 6 and 12 mJy in the 20 cm observing band, and between 7 and 13 mJy in the 13 cm observing band. With our data, we can constrain the frequency at which the pulse disappears to be between 1.9 and 2.3 GHz in the 2010 May 19 epoch.

Fig. 4 shows the pulse profiles, in 200 MHz channels, for the 2010 May 19 epoch. The pulse arrival phase is dependent upon the observing frequency. This dependence is clearly observed for the trailing pulse in the 2009 December 26 epoch (Fig. 5). This frequency dependence is stable over at least six months since we observe similar phenomenon in the trailing pulse in the 2009 December 26 epoch. We determined the arrival phase of the pulses by cross-correlating the single-epoch pulse and the average pulse, and finding the phase of the peak of the cross-correlation. The error of the pulse arrival phase is the variation of the parameter required to increase the reduced χ^2 between the single-epoch pulse and the average pulse by one unit. Table 2 summarizes the arrival phase for the 2010 May 19 epoch.

3 MODELLING

Models for the origin of the pulsed emission from CU Vir have been proposed by Trigilio et al. (2000, 2008, 2011). We perform numerical simulation of each of these models to produce a pulse profile, and compare these with our observations.

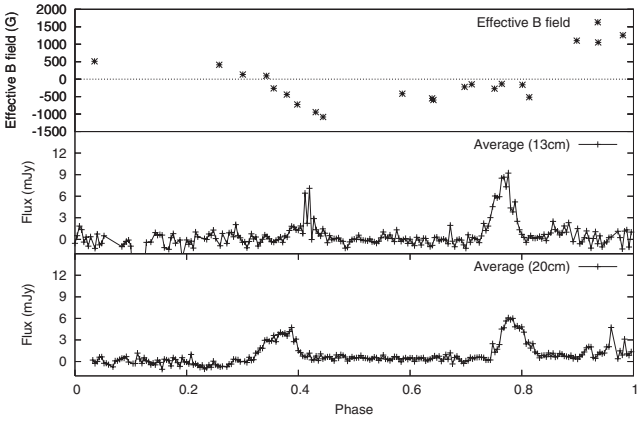

Figure 3. Top: effective magnetic field $B_{\rm eff}$ from Pyper et al. (1998) versus rotation phase. A negative $B_{\rm eff}$ means the field lines are directed into the star. Middle and bottom: average Stokes V pulse profiles at 13 and 20 cm. If we assume CU Vir has a dipolar field structure, then the magnetic south pole is closest to our line of sight during the shorter of the two pulse separations.

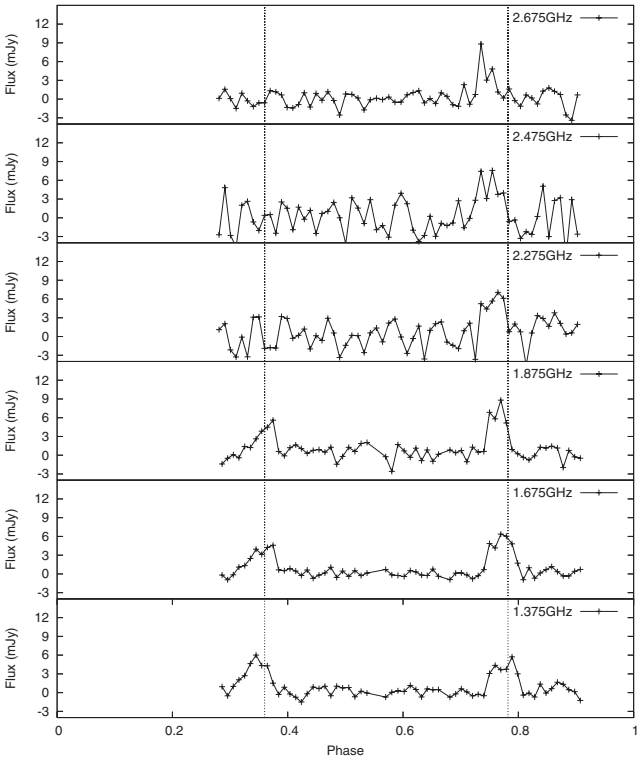

Figure 4. Stokes V pulse profile from the 2010 May 19 epoch. Each panel represents the average of 200 MHz bandwidth. The noise is higher for the three pulse profiles in the 13 cm observing band compared to 20 cm observing band because more channels were removed due to RFI.

3.1 The magnetosphere of CU Vir

The emission models described here are based on a stellar magnetosphere model proposed by Andre et al. (1988), shown in Fig. 6. The cold torus, containing trapped material from the stellar wind, is an extension by Trigilio et al. (2004).

In this model, electrons are accelerated by magnetic reconnection in the magnetic equatorial plane of the star, and propagate along field lines towards the magnetic poles. They are reflected through magnetic mirroring; however, electrons with sufficiently small pitch angles will instead intersect the surface of the star. This results in a loss cone anisotropy in the pitch angles of this population of electrons, allowing them to produce radio emission through the ECM mechanism (Trigilio et al. 2000).

ECM emission occurs close to a harmonic of the cyclotron frequency: $\nu = s\nu_{\rm cyc}$, where s is the harmonic number. We assume the emission to be in the second harmonic, $s = 2$, because the fundamental, $s = 1$, is generally suppressed by gyromagnetic absorption of the thermal plasma in weaker magnetic fields as the radiation escapes, and the growth rates for the higher harmonics are too low for the intensity to be significant (Melrose & Dulk 1982).

The sense of the polarized emission (positive Stokes V; right circular polarization) indicates that it originates entirely from the north magnetic pole of the star. This may be explained by the presence of a quadrupole component in the magnetic field of CU

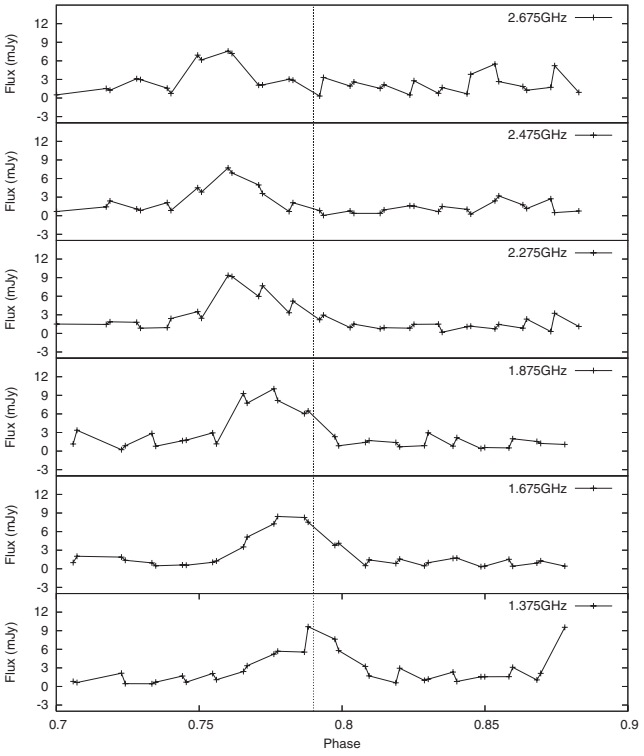

Figure 5. Stokes V pulse profile from the 2009 December 26 epoch. It is clear that the 1.4 GHz pulse lags the 2.7 GHz pulse by ∼0.03 phase.

Table 2. Phases of the leading and trailing pulse in the 2010 May 19 epoch.

Frequency (MHz)	Leading pulse arrival phase	Trailing pulse arrival phase	Pulse separation (h)
1.375	0.360 ± 0.002	0.782 ± 0.002	5.27 ± 0.05
1.675	0.366 ± 0.002	0.778 ± 0.002	5.15 ± 0.05
1.875	0.372 ± 0.006	0.776 ± 0.006	5.1 ± 0.1
2.275	–	0.76 ± 0.02	–
2.475	–	0.76 ± 0.02	–
2.675	–	0.756 ± 0.006	–

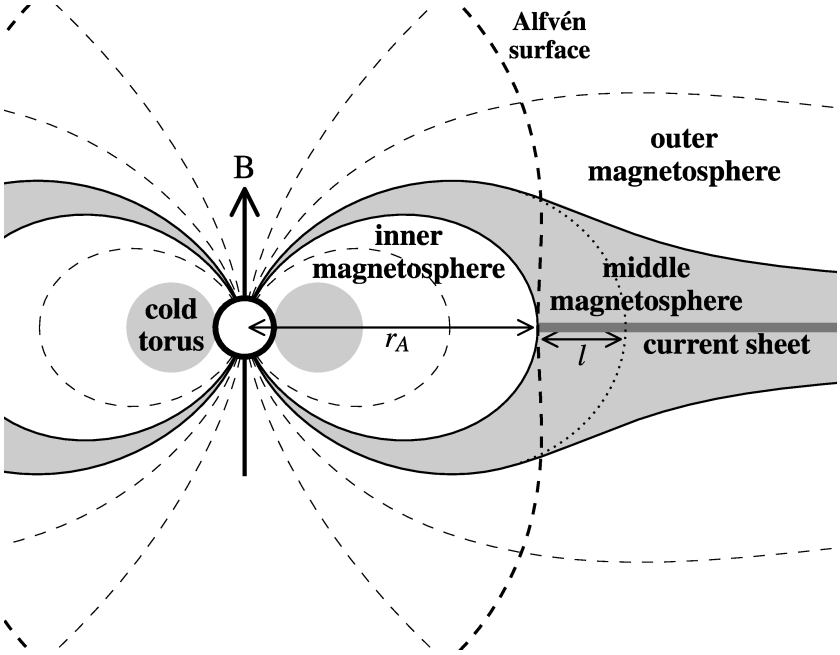

Figure 6. Cross-section of the magnetosphere of CU Vir used in our modelling (not to scale). The magnetic field is assumed to be dipolar within the Alfvén surface (heavy dashes), with equatorial radius r_A. Beyond this radius, field lines (light dashes) are distorted by the stellar wind. Electrons are accelerated in equatorial current sheets beyond the Alfvén radius, and travel along field lines within the middle magnetosphere (shaded), which divides the inner and outer magnetospheres. The parameter l describes the extent of the middle magnetosphere, indicating the position of the projection (dotted) of the field line marking its outer boundary within the Alfvén surface. Cooled gas from the stellar wind accumulates in a torus (shaded) near the star.

Table 3. Adopted parameters for CU Vir.

Parameter	Symbol	Value
Rotation axis inclination (°)	i	43 ± 7^a
Magnetic axis obliquity (°)	β	74 ± 3^a
Stellar radius ($R_\odot$)	R_*	2.2^b
Equatorial Alfvén radius (R_*)	r_A	15 ± 3^c
Thickness of middle magnetosphere (R_*)	l	1.5^c
Dipole moment (A m^2)	m	5.4×10^{33} [d]

[a] Trigilio et al. (2000); [b]North (1998); [c]Leto et al. (2006); [d]see text.

Vir (Trigilio et al. 2000). Consequently, we consider only the north magnetic hemisphere in our modelling.

3.2 Model parameters

Table 3 lists the parameters we use for our modelling. The obliquity of the magnetic axis was calculated by Trigilio et al. (2000) from measurements of the variation in effective magnetic field strength given an inclination i. Leto et al. (2006) derived the Alfvén radius and thickness of the magnetosphere by fitting multifrequency radio flux densities to a three-dimensional magnetospheric model simulating the quiescent gyrosynchrotron emission. The dipole moment is calculated from a value of 3 kG for the magnetic field strength at both poles from Trigilio et al. (2000). Hatzes (1997) suggests an off-centre dipole model, with different surface magnetic field strengths at each pole, but these values give a similar dipole moment.[4] We use only the central value for each parameter, ignoring the uncertainty.

[4] Since the star is treated here simply as a rotating dipolar field, the actual position of its surface is not required for the modelling.

3.3 Emission from field lines parallel to the magnetic axis

The first model for the pulsed emission from CU Vir is from Trigilio et al. (2000). The emission is assumed to be directed as a hollow cone, making an angle of 85° with the local magnetic field. At this point, it was believed that the population of high-energy electrons would approach the star along field lines almost parallel to the magnetic axis, as shown in Fig. 7 (left-hand panel).

Our simulation procedure is as follows.

(i) Select a rotation phase ϕ.

(ii) Determine the magnetic latitude θ_E of emission in the direction of the Earth, using

$$\sin\theta_E = \sin\beta \sin i \cos\phi + \cos\beta \cos i. \quad (1)$$

See Appendix A1 for details.

(iii) Determine the strength of emission in this direction. The emission pattern is a hollow cone making an angle of 85° with the north magnetic axis, i.e. at a magnetic latitude of +5°. We assume the emission to have a narrow Gaussian profile centred on this latitude.

(iv) Repeat steps (i)–(iii) for different rotation phases to form a pulse profile.

A phase of $\phi = 0$ under the definition used in equation (1) corresponds to the point in the rotation of CU Vir when its north magnetic pole is most closely directed towards us. Therefore, we shift the phase by 0.08 to match the ephemeris as described in Section 2. We do not attempt to predict the absolute flux density, but instead scale the peak of the simulated pulse profile to match our observations.

The result of this simulation is shown in Fig. 7 (right-hand panel). This model correctly predicts the arrival times of the pulses. However, it does not fit the width of the pulses, nor their frequency

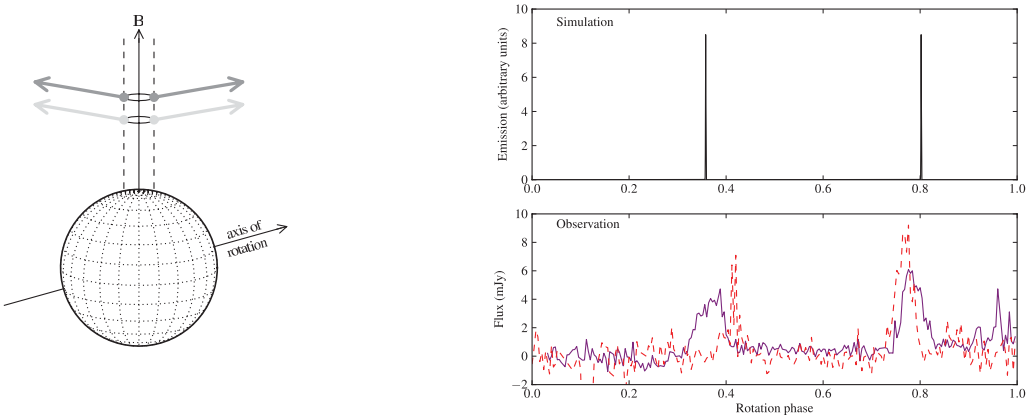

Figure 7. Schematic diagram (left) and pulse profile of emission (right) for the model of ECM emission from field lines (dashed) parallel to the magnetic axis (Section 3.3). The simulated emission in the 20 cm (dark arrows) and 13 cm (light arrows) bands arises from different locations, but is emitted in the same directions, hence producing identical pulse arrival times (top right), in contrast to the averaged observed pulse profile (bottom right). Dotted and solid lines represent the 13 and 20 cm bands, respectively.

dependence (which had not been observed when this model was developed).

3.4 Emission from dipolar magnetic field lines

This model for the pulsed emission from CU Vir is from Trigilio et al. (2008). It incorporates results from Leto et al. (2006), who determined parameters of the magnetosphere, including the Alfvén radius $r_{\rm A}$. These values imply that the field lines of the middle magnetosphere near the star are not parallel to the magnetic axis. We assume them to have a dipolar configuration, as shown in Figs 6 and 9 (left-hand panel).

Our simulation procedure is as follows.

(i) Select a rotation phase and convert to magnetic latitude, as in Section 3.3.

(ii) Select a point on the magnetic equator at radius $r_{\rm A}$.

(iii) From this point, trace along the field line towards the north magnetic pole, following the path that would be taken by an electron in the middle magnetosphere.

(iv) At each point along the field line, determine the cyclotron frequency. When the cyclotron frequency is equal to half of the required emission frequency (corresponding to emission at the second harmonic), stop and note the magnetic latitude θ_B of the direction of the magnetic field at this point.

(v) The emission is assumed to be directed as a hollow cone centred on an axis with magnetic latitude θ_B. We determine the parameter ω which describes the position of the emission vector on this cone, as shown in Fig. 8:

$$\cos\omega = \frac{\sin\theta_{\rm E} - \cos\delta\sin\theta_B}{\sin\delta\cos\theta_B}. \quad (2)$$

(vi) If there was no solution for ω, the emission power P in this direction is zero. Otherwise, the emission power per solid angle Ω is

$$\frac{{\rm d}P}{{\rm d}\Omega} \propto \frac{1}{\sin\omega\cos\theta_B\sin\delta}. \quad (3)$$

This formula is obtained by assuming the emission power to be equally distributed around the cone. See Appendix A2 for details.

(vii) Repeat steps (i)–(vi) for different rotation phases to form a pulse profile.

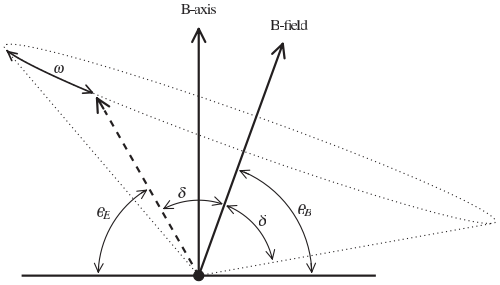

Figure 8. Emission in a hollow cone (dotted) centred on a magnetic field vector ('B-field') at a magnetic latitude of θ_B. The half-opening angle of the cone is δ. A sample emission vector is shown as a dashed arrow. This vector may be parametrized with the angle ω, which describes its position on the cone. Equation (2) describes the relationship between ω and the magnetic latitude of the emission, $\theta_{\rm E}$.

(viii) Repeat steps (i)–(vii) for different values of δ. Sum the resulting profiles, weighting them with a narrow Gaussian function centred on $\delta = 85^\circ$.

(ix) Repeat steps (i)–(viii) for emission frequencies across the observation band. Sum the resulting profiles, weighting them equally.

(x) Repeat steps (i)–(ix) for starting points on the magnetic equator with radii between $r_{\rm A}$ and $r_{\rm A} + l$. Sum the resulting profiles, weighting them equally.

The phase and height of the pulse profile are then adjusted as in Section 3.3. The Gaussian function used in step (viii) is very narrow (width $<0\overset{\circ}{.}2$), intended only to smooth over the step size in other parameters, so the width of the resulting profile is due to other aspects of the model.

Results are shown in Fig. 9 (right-hand panel). The simulated pulses are too wide to fit the observations, and display a distinct double-peaked structure which is absent in the real data. There is some frequency dependence, but it affects the pulse width (narrower at higher frequency) rather than the arrival time.

3.5 Refracted equatorial emission

This model for the pulsed emission from CU Vir is from Trigilio et al. (2011). Rather than a hollow cone centred on the local field line, the ECM emission is assumed to be directed perpendicular to the local field line, and only in the two directions which are also

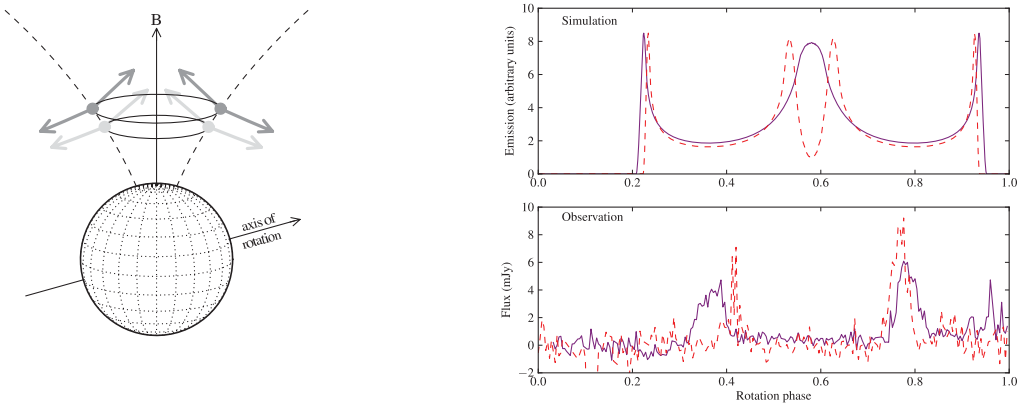

Figure 9. Schematic diagram (left) and pulse profile of emission (right) for the model of ECM emission from field lines diverging from the magnetic axis (Section 3.4). The regions in the magnetosphere where emission occurs are marked with solid rings, and the dark and light arrows correspond to emission in the 20 and 13 cm bands. The simulated emission (top right) is spread over a very broad range of magnetic latitudes, resulting in an extended pulse profile quite distinct from our averaged observations (bottom right). Dotted and solid lines represent the 13 and 20 cm bands, respectively.

parallel to the magnetic equatorial plane. For each longitude in the magnetic equatorial plane, this results in emission being visible from two points in the emission region.

The key point of this model is that it includes the effect of refraction as the radiation crosses the boundary of the cold torus region (Fig. 6). We neglect the effects of refraction from density variations within the cold torus, or from the interface where the radiation exits the torus. The refractive index outside the cold torus is assumed to be unity. Inside the torus, the refractive index $n_{\rm ct}$ depends on the orientation of the magnetic field relative to the radiation (Gurnett & Bhattacharjee 2005), but if we assume them to be parallel it is

$$n_{\rm ct} = \sqrt{1 - \frac{\nu_{\rm p}^2}{\nu(\nu - \nu_{\rm cyc})}}. \quad (4)$$

For a plasma density in the cold torus of $10^9\,{\rm cm}^{-3}$, compatible with Leto et al. (2006), the plasma frequency is $\nu_{\rm p} = 280\,{\rm MHz}$. If we assume that the magnetic field strength at the point of refraction is approximately the same as that at the point of emission, we have the cyclotron frequency $\nu_{\rm cyc} = \nu/2$ (if the emission is at the second harmonic).

If the angle of incidence $\alpha_{\rm i}$ with the boundary of the torus (see Fig. 10) is assumed to be 60°, as by Trigilio et al. (2011), the angle of refraction $\alpha_{\rm R}$ can be found with Snell's law:

$$\sin\alpha_{\rm R} = \frac{1}{n_{\rm ct}} \sin\alpha_{\rm i}. \quad (5)$$

For $n_{\rm ct} < \sin\alpha_{\rm i}$, this implies that the radiation is entirely reflected at the interface, and none is transmitted. Under the conditions assumed here, this occurs for $\nu < 790\,{\rm MHz}$, so the pulse spectrum should be truncated below this frequency. However, this is below the frequency range of our observations, so we cannot test this here.

Our simulation procedure is as follows.

(i) Select a rotation phase and convert to magnetic latitude, as in Section 3.3.

(ii) Convert from the magnetic latitude of the emission to the angle of refraction. From our assumption about the angle of incidence, this is done by adding 60°.

(iii) Calculate the refractive index at this frequency with equation (4).

(iv) Determine the angle of incidence with equation (5).

(v) Convert from the angle of incidence to the original magnetic latitude of the emission. From our assumption about the angle of incidence, this is done by subtracting 60°.

(vi) Determine the strength of emission in this direction. We assume the emission to have a narrow Gaussian profile centred on the magnetic equator.

(vii) Repeat steps (i)–(vi) for different rotation phases to form a pulse profile.

(viii) Repeat steps (i)–(vii) for emission frequencies across the observation band. Sum the resulting profiles, weighting them equally.

The phase and height of the pulse profile are then adjusted as in Section 3.3. The Gaussian function used in step (vi) is very narrow (width $<0.^{\circ}2$), so the width of the resulting profile is due to variation with frequency across the observation band.

Results are shown in Fig. 10 (right-hand panel). The pulse arrival times and their frequency dependence both fit the observations. The observed pulses are wider than the simulated pulses; this may be due to inherent width of the emission beam, variation of the angle of incidence or further turbulent refraction in the cold torus.

4 CONCLUSIONS

We observed CU Vir with the ATCA over six epochs and, in the 20 cm observing band, detected 100 per cent circularly polarized pulses twice in a rotation period. This confirms that the 20 cm pulses are stable over a period of more than a decade. We did not detect the 13 cm leading pulse that was observed a year earlier by Ravi et al. (2010). For our data, the leading pulse has a spectrum which cuts off between 1.9 and 2.3 GHz. We can see a clear frequency dependency in the time between leading and trailing pulses across our entire observing band.

We have simulated in detail the emission models proposed by Trigilio et al. (2000, 2008, 2011). We show that the first two models do not fit our observations, the first being excluded by its lack of frequency dependence and the second by its grossly dissimilar pulse profile. We confirm that the third model, involving refraction of the emission as it propagates through material in the stellar magnetosphere, yields the correct frequency dependence and pulse arrival times to fit our observations.

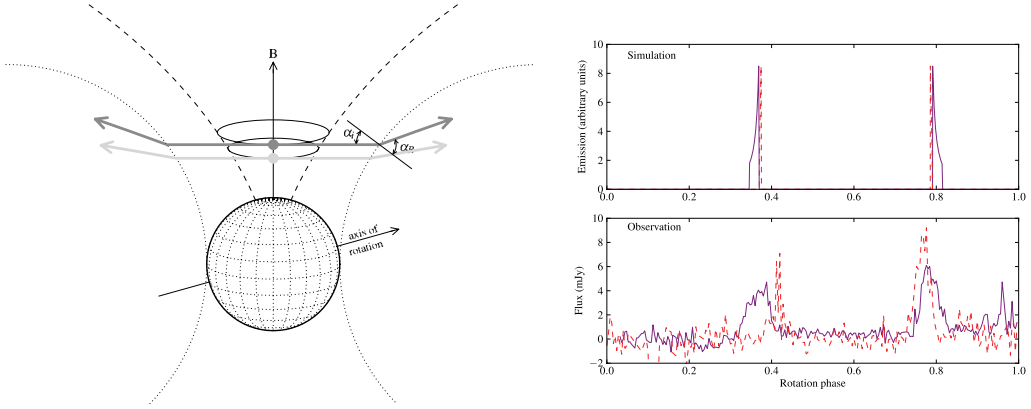

Figure 10. Schematic diagram (left) and pulse profile of emission (right) for the model of refracted ECM emission in the equatorial plane (Section 3.5). The regions in the magnetosphere where emission occurs are marked with solid rings. The emission in the 20 and 13 cm bands (dark and light arrows, respectively, and solid and dotted lines on the right) is refracted as it crosses the boundary of the cold torus region (dotted). This results in frequency dependence in the pulse arrival time, corresponding with the observations (bottom right). Note that the refraction in the left-hand panel is exaggerated.

ACKNOWLEDGMENTS

The Australia Telescope Compact Array is part of the Australia Telescope which is funded by the Commonwealth of Australia for operation as a National Facility managed by CSIRO. KKL is supported by an Australian Postgraduate Award and a CSIRO OCE scholarship. KKL and BMG acknowledge the support of the Australian Research Council through grant DP0987072. The Centre for All-sky Astrophysics is an Australian Research Council Centre of Excellence, funded by grant CE11E0090. GH is the recipient of an Australian Research Council QEII Fellowship (no. DP0878388). VR is the recipient of a John Stocker Postgraduate Scholarship from the Science and Industry Endowment Fund. KKL would like to thank Robert Braun for helpful discussions. We are grateful to Bernie Walp for performing one of our observations.

REFERENCES

Andre P., Montmerle T., Feigelson E. D., Stine P. C., Klein K., 1988, ApJ, 335, 940
Borra E. F., Landstreet J. D., 1980, ApJS, 42, 421
Deutsch A. J., 1952, ApJ, 116, 536
Drake S. A., Abbott D. C., Bastian T. S., Bieging J. H., Churchwell E., Dulk G., Linsky J. L., 1987, ApJ, 322, 902
Gurnett D., Bhattacharjee A., 2005, Introduction to Plasma Physics. Cambridge Univ. Press, Cambridge
Hatzes A. P., 1997, MNRAS, 288, 153
Leone F., 1991, A&A, 252, 198
Leone F., Umana G., 1993, A&A, 268, 667
Leone F., Trigilio C., Umana G., 1994, A&A, 283, 908
Leone F., Umana G., Trigilio C., 1996, A&A, 310, 271
Leto P., Trigilio C., Buemi C. S., Umana G., Leone F., 2006, A&A, 458, 831
Linsky J. L., Drake S. A., Bastian T. S., 1992, ApJ, 393, 341
Melrose D. B., Dulk G. A., 1982, ApJ, 259, 844
North P., 1998, A&A, 334, 181
Pyper D. M., Ryabchikova T., Malanushenko V., Kuschnig R., Plachinda S., Savanov I., 1998, A&A, 339, 822
Ravi V. et al., 2010, MNRAS, 408, L99
Sault R. J., Teuben P. J., Wright M. C. H., 1995, in Shaw R. A., Payne H. E., Hayes J. J. E., eds, ASP Conf. Ser. Vol. 77, Astronomical Data Analysis Software and Systems IV. Astron. Soc. Pac., San Francisco, p. 433
Trigilio C., Leto P., Leone F., Umana G., Buemi C., 2000, A&A, 362, 281
Trigilio C., Leto P., Umana G., Leone F., Buemi C. S., 2004, A&A, 418, 593
Trigilio C., Leto P., Umana G., Buemi C. S., Leone F., 2008, MNRAS, 384, 1437
Trigilio C., Leto P., Umana G., Simona Buemi C., Leone F., 2011, ApJ, 739, L10
Wilson W. E. et al., 2011, MNRAS, 416, 832

APPENDIX A: ANGULAR RELATIONS

A1 Rotation of CU Vir

Equation (1) connects the rotation phase of CU Vir to the magnetic latitude of emission in the direction of the Earth. The relation between these is shown, with associated angles and unit vectors, in Fig. A1. To derive the relationship, we construct vectors

$$\boldsymbol{U} = \hat{\boldsymbol{E}} - (\hat{\boldsymbol{E}} \cdot \hat{\boldsymbol{S}})\hat{\boldsymbol{S}},$$

$$\boldsymbol{V} = \hat{\boldsymbol{B}} - (\hat{\boldsymbol{B}} \cdot \hat{\boldsymbol{S}})\hat{\boldsymbol{S}},$$

with lengths

$$|\boldsymbol{U}| = \sin i$$

$$|\boldsymbol{V}| = \sin \beta.$$

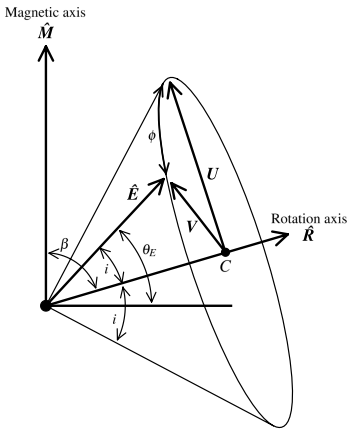

Figure A1. Rotation of CU Vir. The magnetic axis $\hat{\boldsymbol{M}}$ and the rotation axis $\hat{\boldsymbol{R}}$ are inclined by β. In the reference frame of the star, the vector towards the Earth $\hat{\boldsymbol{E}}$ describes a circle around point C on the rotation axis, separated from the rotation axis by i, and parametrized by the rotation phase ϕ. The magnetic latitude of this vector is $\theta_{\rm E}$. The vectors $\boldsymbol{U}$ and $\boldsymbol{V}$ are in the planes $\hat{\boldsymbol{R}}$–$\hat{\boldsymbol{M}}$ and $\hat{\boldsymbol{R}}$–$\hat{\boldsymbol{E}}$, respectively; for their application, see Section A1.

The angle between these vectors is ϕ, which we can then find as

$$\cos\phi = \frac{\boldsymbol{U}\cdot\boldsymbol{V}}{|\boldsymbol{U}||\boldsymbol{V}|} = \frac{\hat{\boldsymbol{E}}\cdot\hat{\boldsymbol{B}} - (\hat{\boldsymbol{E}}\cdot\hat{\boldsymbol{S}})(\hat{\boldsymbol{S}}\cdot\hat{\boldsymbol{B}})}{\sin i \sin\beta}. \quad \text{(A1)}$$

As $\hat{\boldsymbol{E}}$, $\hat{\boldsymbol{S}}$ and $\hat{\boldsymbol{B}}$ are unit vectors, we can evaluate these dot products as trigonometric identities:

$$\cos\phi = \frac{\sin\theta_{\rm E} - \cos i\cos\beta}{\sin i\sin\beta}. \quad \text{(A2)}$$

Rearranging, we obtain

$$\sin\theta_{\rm E} = \sin\beta\sin i\cos\phi + \cos\beta\cos i, \quad \text{(A3)}$$

which is the same as equation (1).

A2 Conical emission

Step (v) of the procedure in Section 3.4 assumes a relation, equation (2), between the magnetic latitude of emission $\theta_{\rm E}$ and the position ω of that emission on a cone, as shown in Fig. 8. To demonstrate this, we note that Fig. A1 is equivalent to Fig. 8, with the following substitutions:

$$\beta \rightarrow \frac{\pi}{2} - \theta_B,$$
$$i \rightarrow \delta,$$
$$\phi \rightarrow \omega.$$

Therefore, the derivation of equation (A2) in Section A1 also demonstrates the correctness of equation (2):

$$\cos\omega = \frac{\sin\theta_{\rm E} - \cos\delta\sin\theta_B}{\sin\delta\cos\theta_B}. \quad \text{(A4)}$$

In step (vi), we then wish to find the emission power P per solid angle Ω in this direction. We may assume that the emission is evenly distributed around the cone (i.e. $\mathrm{d}P/\mathrm{d}\omega$ is constant). If we differentiate equation (A4) with respect to $\theta_{\rm E}$, we get

$$\frac{\mathrm{d}\omega}{\mathrm{d}\theta_{\rm E}} = -\frac{\cos\theta_{\rm E}}{\cos\theta_B\sin\delta\sin\omega}. \quad \text{(A5)}$$

This allows us to obtain the distribution of emission power with magnetic latitude:

$$\frac{\mathrm{d}P}{\mathrm{d}\theta_{\rm E}} = \frac{\mathrm{d}P}{\mathrm{d}\omega}\frac{\mathrm{d}\omega}{\mathrm{d}\theta_{\rm E}} \propto -\frac{\cos\theta_{\rm E}}{\cos\theta_B\sin\delta\sin\omega} \quad (\text{as } \frac{\mathrm{d}P}{\mathrm{d}\omega} \text{ is constant}). \quad \text{(A6)}$$

The emission power per solid angle is related to this as

$$\frac{\mathrm{d}P}{\mathrm{d}\Omega} = \frac{1}{2\pi}\frac{1}{\cos\theta_{\rm E}}\frac{\mathrm{d}P}{\mathrm{d}\theta_{\rm E}} \propto \frac{1}{\cos\theta_B\sin\delta\sin\omega}. \quad \text{(A7)}$$

This is the result used in step (vi) of Section 3.4: equation (3).

This paper has been typeset from a TEX/LATEX file prepared by the author.